



Experimental determination of noble gases and SF₆, as tracers of CO₂ flow through porous sandstone

R. Kilgallon*, S.M.V. Gilfillan, K. Edlmann, C.I. McDermott, M. Naylor, R.S. Haszeldine

The University of Edinburgh, School of GeoSciences, Grant Institute, James Hutton Road, EH9 3FE, Scotland

ARTICLE INFO

Keywords:

Breakthrough curves
CO₂
Monitoring
Noble gases
Porous media
Tracers

ABSTRACT

In order to label the CO₂ injected underground for geological storage and allow it to be differentiated from natural sources, a panoply of additive chemical tracers have been proposed. Yet, the transport of these tracers relative to CO₂ in pore space is currently poorly constrained. This leads to uncertainty as to whether tracers will act as an early warning of CO₂ arrival, or be preferentially retained in the pore space making them ineffective. Here, we present the factors affecting transport of noble gases and SF₆ relative to CO₂ in a porous rock. Using a porous sandstone core, each of the tracers were loaded into a sample loop and injected as discrete gas pulses into a CO₂ carrier stream at five different experiment pressures (10–50 kPag upstream to ambient pressure downstream). Tracer arrival profiles were measured using a quadrupole mass spectrometer. Significantly, our results show that peak arrival times of helium were slower than the other noble gases at each pressure gradient. The differences in peak arrival times between helium and other noble gases increased as the pressure gradient along the system decreased and the curve profiles for each noble gas differ significantly. The heavier noble gases (Kr and Xe) along with SF₆ show an earlier arrival time and a wider curve profile compared to He and Ne curves through the CO₂ carrier gas stream. This shows that Kr and Xe could be substituted for SF₆, a potent greenhouse gas, in tracer applications. For comparison, CO₂ pulses were passed through a N₂ carrier gas resulting in significantly slower peak arrival times compared to those of noble gases and SF₆. Hence, all investigated tracers when co-injected with CO₂ could potentially act as early warning tracers of CO₂ arrival, though we find that Kr, Xe and SF₆ will provide the most robust advance warning. Analysis of our experimental results shows that they cannot be explained by a simple one dimensional flow model through a porous medium. We outline a conceptual model that incorporates different preferential flow paths depending on flow velocities of individual gas streams. This model can explain the observed dataset and shows that the flow of noble gases and SF₆ tracers is influenced by pore-scale heterogeneity.

1. Introduction

Increases in the atmospheric concentration of greenhouse gases and aerosols alter the energy balance of the climate system (IPCC, 2015). CO₂ is the second most abundant greenhouse gas in the Earth's atmosphere after H₂O and a major contributor to radiative forcing. The primary source of the increased atmospheric concentration of CO₂ since the preindustrial period is from the combustion of fossil fuels, a significant source of global energy for decades to come (Haszeldine, 2009). Thus it is imperative that the levels of CO₂ emitted from fossil fuel combustion are significantly reduced, an essential goal to limit the increase in global average temperature to below 2 °C above pre-industrial levels (UNFCCC, 2015).

Carbon Capture and Storage (CCS) is the only currently available technology that can directly reduce the emissions from power

generation and industrial point sources. Combined with biomass combustion (BECCS) it also offers the potential of net removal of CO₂ from the atmosphere (Azar et al., 2010). Industrial scale carbon capture and storage technologies rely on the secure long term storage of CO₂ in the subsurface (Miocic et al., 2016). The engineering, long-term safety and social licence to operate a geological storage site is critically dependent on how secure CO₂ retention is assessed and communicated. Hence, there is a need for robust monitoring regimes, which can detect any unplanned migration of CO₂ during storage. The unplanned migration of CO₂ does not necessarily imply that the storage site has failed, thus there is a difference between migration and leakage. Leakage implies that during migration, the CO₂ enters environmentally sensitive regions (e.g. groundwater aquifers, or escaping to the surface) where it may result in damage to the environment, human health or release back into the atmosphere. Migration means the movement of CO₂ out of the

* Corresponding author.

E-mail addresses: kilgallonrachel@gmail.com (R. Kilgallon), stuart.gilfillan@ed.ac.uk (S.M.V. Gilfillan).

<http://dx.doi.org/10.1016/j.chemgeo.2017.09.022>

Received 27 November 2016; Received in revised form 5 August 2017; Accepted 15 September 2017

0009-2541/ © 2017 The Authors. Published by Elsevier B.V. This is an open access article under the CC BY-NC-ND license (<http://creativecommons.org/licenses/by-nc-nd/4.0/>).

Nomenclature

μ	dynamic viscosity of the fluid
A	pore area
D	pore diffusion coefficient
D_x	longitudinal apparent diffusion constant
ρ_f	density of the fluid
i	hydraulic head/gradient
K	hydraulic conductivity
k	intrinsic permeability
L	characteristic length
M_0	mass injected
P	pore perimeter

n_e	effective porosity
q	specific discharge
Re	Reynolds number
t	time
v	advective velocity
v_f	velocity of the fluid
x	flow path length
α	dispersivity
α^*	non-linear flow parameter (Forchheimer equation)
β	turbulence factor (Forchheimer coefficient)
γ	pore geometry
ρ	fluid density

intended subsurface storage site, but that CO₂ is still retained in the subsurface and does not leak to the surface. Monitoring a CO₂ storage site before, during and after injection is crucial part of the regulatory framework for CCS. Continuous monitoring of a site and the surrounding environment minimises the potential risk of leakage of CO₂, as well as improving the opportunity to mitigate any changes that may occur over time, helping with the social licence to operate the storage site (Haszeldine, 2009; Scott et al., 2013).

The term ‘chemical monitoring’ in application to CO₂ storage refers specifically to a substance (solid, liquid or gas) that can be measured to characterise it before, during and after the monitoring process. A chemical tracer can be any substance used to understand the physical movements of fluid through a system. It has been shown that chemical tracers can be complementary to physical monitoring methods (Myers et al., 2013). The majority of tracer applications within CCS are related to either understanding the subsurface, quantifying the trapping capacity or determining containment and leakage rates for monitoring (Myers et al., 2012). The main advantages of chemical tracers are that they can be used to make measurements that are difficult to access physically and can cover large scales. Monitoring injected CO₂ can be challenging, as it is a reactive compound, highly soluble and its properties are dependent on the pressure and temperature of the system. Thus, the use of non-reactive conservative chemical tracers that have limited interactions with the injection fluids and surrounding reservoir, enable the tracking of fluid pathways. Such tracers include synthetic chemicals such as SF₆ and perfluorocarbon tracers (PFTs), isotopic labelled gases and noble gases. Such tracers have been used to track the movement and fate of injected CO₂ in a variety of CO₂ injection experiments, injecting Frio, Otway and Cranfield (McCallum et al., 2005; Jenkins et al., 2012; Lu et al., 2012).

Noble gases (He, Ne, Ar, Kr and Xe) exist in trace amounts in geological environments and they can be used as tracers within natural CO₂ reservoirs (Gilfillan et al., 2008; Gilfillan et al., 2009; Zhou et al., 2012; Sathaye et al., 2014) and for CO₂ used in EOR projects (Nimz and Hudson, 2005; Györe et al., 2015; Györe et al., 2017). As such, small amounts of noble gas blends can also be intentionally added to the CO₂ being injected for storage or be measured in the captured CO₂ stream and used as tracers to monitor CO₂ movement (Hovorka et al., 2013; Flude et al., 2016; Flude et al., 2017). This distinct mixture of noble gas isotopic compositions can be identified during monitoring as being associated with the injected CO₂. To investigate the potential role of noble gases as tracers for CO₂ storage the physical behaviours of noble gases and CO₂ within the porous media needs to be fully understood.

Furthermore, recent work on the flow of N₂ and brine through a permeable sandstone at subsurface reservoir conditions has shown that Darcy flow conditions are not maintained and instead the flow undergoes ‘dynamic connectivity’ (Reynolds et al., 2017) emphasising that we do not yet fully understand the complexity of fluid flow through ‘real world’ heterogeneous porous media.

A common method to observe the behaviour of fluids under

laboratory conditions is to carry out one dimensional flow through column experiments; these columns can be built from cores of natural rock or artificially constructed using materials such as packed silica beads (Edlmann et al., 2013; Liu et al., 2014). In this study a specially constructed flow cell was designed and built to investigate how noble gases could be used as tracers for CO₂ migration in storage sites. From this equipment, experimental breakthrough curves for noble gases travelling through a sample of porous sandstone in relation to CO₂ over pressure gradients of 10, 20, 30, 40 and 50 kPa were generated (10–50 kPag upstream to ambient pressure downstream) at laboratory temperature. For comparative purposes the same experiments were conducted for SF₆, another popular fluid tracer. Here, we present the results from these experiments, which were then modelled using a one dimensional advective dispersion transport equation. The outcome of these results is then explained in terms of a preferential pathway system, where the relative contribution of the flow paths depend on comparative flow velocity differences.

2. Experimental methods

2.1. Sample characterisation

A representative sample of porous media was required to characterise the transport behaviours of noble gases, SF₆ and CO₂ under the same experimental conditions. A sample of sandstone was then selected. The sample was quarried at South Charlton, near Alnwick in Northumberland and is commercially referred to as the Hazeldean sandstone (Hutton Stone Co. Ltd., 2013). The sandstone is part of the Fell Formation that is Chadian to Holkerian (Carboniferous) in age (British Geological Survey, 2016). The sandstone is massive and it was selected due to its high quartz content (~95%) and the low carbonate content (trace amounts).

The Fell sandstone sample was subjected to analysis prior to the commencement of experiments. When the trace minerals were discounted, XRD results indicate that the Fell sandstone is mostly comprised of quartz (95%), with minor feldspar and clay minerals and is a quartz arenite, as previously classified (Bell, 1978). A 3.8 cm × 7 cm cylindrical plug was used to identify the porosity and permeability of the sandstone. The porosity was determined using a helium gas expansion porosimeter. The permeability was determined using a nitrogen gas permeameter. Initial laboratory testing of the sandstone provided a porosity of 20.3% and a permeability of 221.33 mD.

Understanding the pore network of the Fell sandstone is advantageous when evaluating the mechanisms involved in the transport of noble gases, SF₆ and CO₂ tracers. Hence, extensive mapping of the pore network connectivity of the sample from images was conducted. The pore network, distribution and interactions within the rock were investigated using image analysis (via ImageJ at <https://imagej.nih.gov/ij/index.html>).

Data from four thin sections are presented using this image

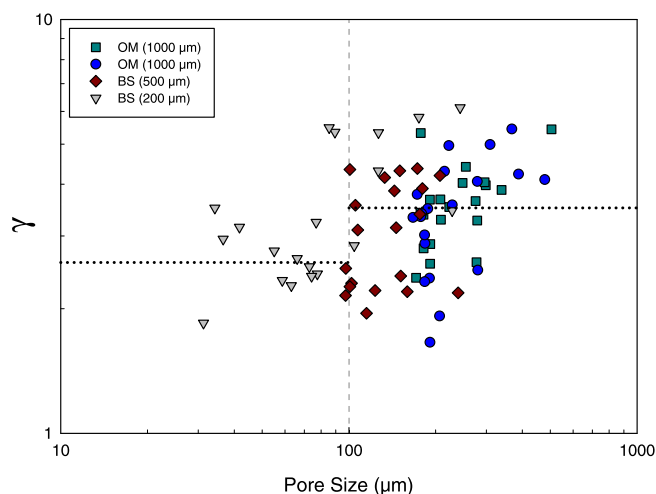


Fig. 1. Plot of pore shape parameter (γ) with the macro pore space ($> 10 \mu\text{m}$) for individual pores of the Fell sandstone. The plot presents the image analysis of four images taken at three magnifications (1000, 500 and 200 μm). The 20 largest area pores spaces were chosen from each of the four images. The dotted line represents the median value taken for each pore space range (2.59 for 10–100 μm and 3.51 for 100–1000 μm). The median values suggest that the smaller pores are simple and well rounded; but become more complex and branched with an increase in size (Anselmetti et al., 1998).

processing programme: two optical microscope (OM) sections and two backscatter sections (BS) were used. The two OM sections were scaled at 1000 μm ; the BS images used were 500 μm and 200 μm . The different image sources were chosen to identify any changes in pore network with scale.

For this research the relation between pore length and pore area is simplified by defining the pore length as the square root of the pore area. Consequently, the pore area value measured by the image analysis programme can be converted to a pore length value. Based on existing literature, pore shape analysis was completed on the images obtained from the OM and BS images (Anselmetti et al., 1998):

$$\gamma = \frac{P}{2\sqrt{\pi A}} \quad (1)$$

γ is a dimensional value that represents the pore geometry. A spherical pore is seen as a circle in a 2D image and would have a γ value equal to one. Pore spaces will become more complex and diverging as the γ value increases. The input P is part of the results produced during the particle analysis.

For this analysis twenty pores with the largest areas from each of the images were measured. Fig. 1 shows the calculated pore size diameter measured against γ . The dotted line represents the median value taken for each pore space range and shows that the smaller pores have lower γ values. These median values suggest that the smaller pores are simple and well-rounded but become more complex with increasing size (Anselmetti et al., 1998). These results suggest there are some simple pores present as well as some highly branching pathways.

2.2. Equipment design and method

A flow cell was designed and constructed to determine the breakthrough curves of tracers in the gaseous phase over a range of low pressure gradients through the Fell sandstone. A schematic diagram of the experiment apparatus is shown in Fig. 2. The apparatus was constructed from a series of 1/16" stainless steel pipe, which allows a pulse of tracer gas to be loaded and released at a determined time through a feeder gas. This gas travels through the core where it is sampled downstream by a Hiden quadrupole mass spectrometer (QMS). The entire system is subdivided into a sample tracer loop section, a feeder gas section, a purging section and a flow cell/end plate design

that contains the porous media.

This experimental set up was used to complete a series of pulse release experiments using noble gases and SF₆ tracers using CO₂ as a carrier gas over a range of five low pressures gradients within the core (10–50 kPag upstream to ambient pressure downstream). For comparative purposes, experiments were also carried out under the same experimental conditions for CO₂ using N₂ as a carrier gas. Each of the pulse release experiments were repeated five times for each of the sampling pressures. From these repeat experiments a representative breakthrough curve was produced for each of the gases.

The sandstone used in the flow cell was allowed to naturally air-dry before its construction. Prior to each experiment commencement, the system was flushed using the feeder gas. The system purge time was based on the estimated pore volume of the core and the flow rate of 0.2 SL min⁻¹, such that the core was replaced with a new volume of purging gas every minute. This is carried out for 30 min prior to every experiment to ensure that any gas that may be trapped in pore end space was also purged. The QMS was used to confirm the removal of any other gases except for the feeder gas. During the experiment, the upstream pressure gradient is monitored and maintained using digital pressure gauges (accuracy $\pm 0.25\%$ full scale).

2.3. Further analysis of the porosity and permeability of the system

Using experimental outputs, permeability values were measured for the flow cell sample. Permeability was calculated using the incompressible flow equation assuming linear Darcy flow (Carman, 1956). Flow rates were measured using a Cole-Parmer acrylic flowmeter kit. Table 1 shows the permeability range calculated from the pressure end-members during the experiments.

Further permeability and porosity values were estimated using the BS images and the generated 3D pore network image are compared to the ImageJ output in Table 2. The PAM results provided much lower permeability values than the plug and experimentally derived values. These major differences found in the permeability values are most likely the result of scale and relative sample sizes. The PAM images were produced using BS images and compared to the scale of the experiments (~ 1 m length), and could miss the larger pores that behave as preferential flow paths. It is also possible that the permeability values are lower due to the use of a single binaries image to construct the PAM. Ideally, three orthogonal images would preserve the directionality of the model (van der Land et al., 2013) and this could have affected the

Table 1

Calculated permeability values for the Fell sandstone core under experimental conditions using incompressible flow (Carman, 1956). The accuracy of this flowmeter was $\pm 5\%$ full scale (± 0.05 SL min⁻¹).

Pressure (kPa)	Permeability (k)		Flow Rate (Q) (m ³ s ⁻¹)	Error (Q) (m ³ s ⁻¹)
	(m ²)	(mD)		
50	9.31×10^{-13}	943.71	3.33×10^{-6}	$\pm 8.33 \times 10^{-7}$
10	1.16×10^{-12}	1179.63	8.33×10^{-7}	

Table 2

Results of permeability and porosity values generated from PAM analysis (by the Institute of Petroleum Engineering, Heriot-Watt University). For comparison, the ImageJ values for the same field of view and the plug results (Plug) have been included.

Sample (μm)	Permeability (k) (mD)		Porosity (n_v) (%)			
	PAM	Plug	PAM	Image	Plug	ImageJ
500	34.61	221.33	14.49	16.34	20.3	14.65
200	4.43	221.33	15.28	15.28	20.3	19.78

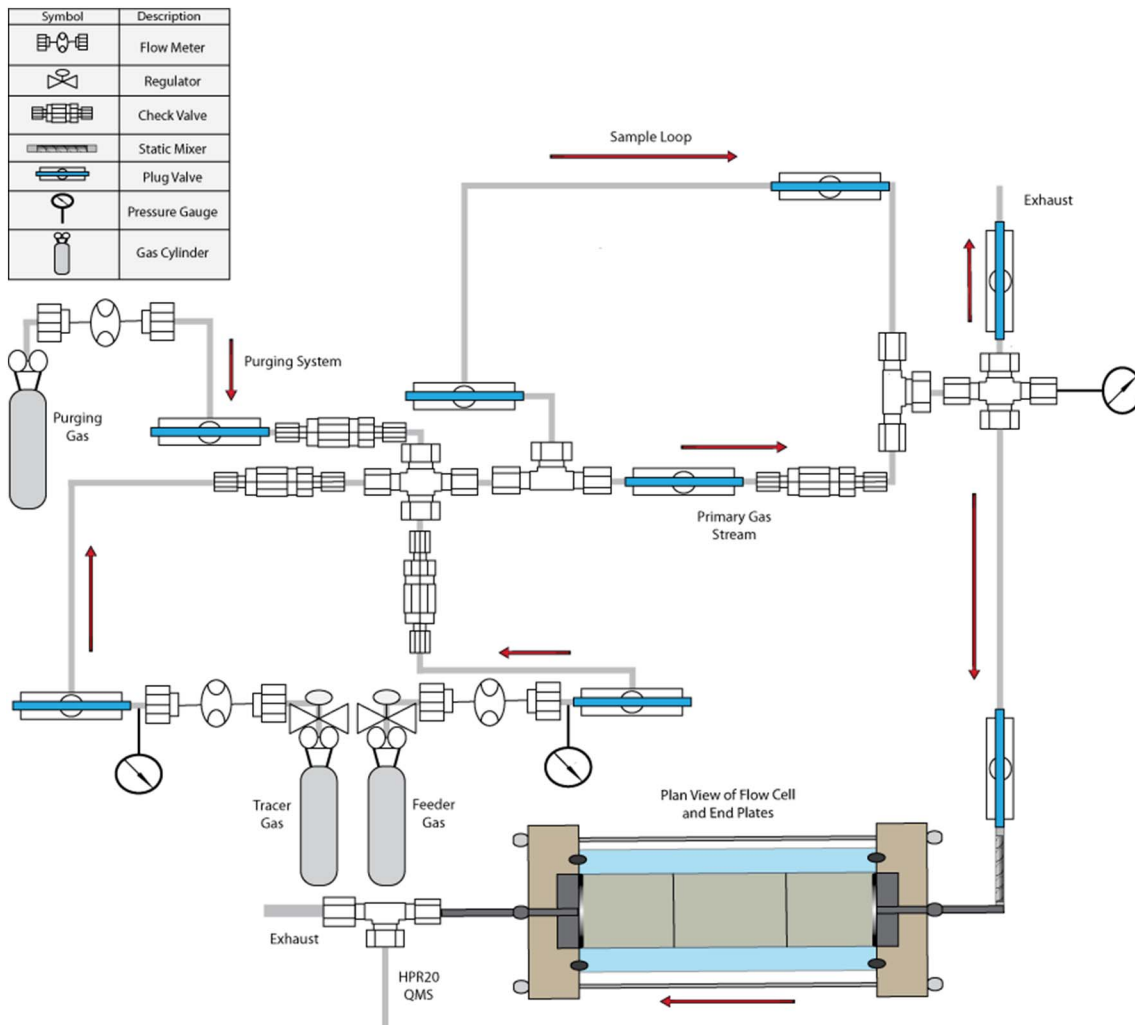


Fig. 2. Schematic diagram of the layout of experimental equipment used for tracer flow experiments.

permeability results. Additionally, the binarisation of the BS images can be a source of error as highlighted with the ImageJ analysis, which may reduce the connectivity of pores.

The porosity estimations obtained from the images using ImageJ are a close comparison to those estimated by PAM images and the slight differences can be attributed to the different techniques that set the detection thresholds.

3. Results

3.1. Experimental results

Pulse release experiments were carried out over five low pressure gradients within the core (10–50 kPag upstream to ambient pressure downstream). At each pressure value, the experimental procedure was repeated 5 times. From these repeat experiments a representative breakthrough curve was produced. To compare the results across the experiments, it was necessary to normalise all the values. Prior to pulse release, baseline values were recorded from background readings for each experiment. These values were deducted from the output values from each experiment. The corrected curves were plotted using C/C_{\max} , with C/C_{\max} being the current value (or concentration) of the gas at a given time over the peak value obtained during the experiment. Plotting all results as C/C_{\max} , allows for direct comparison of the result profiles for each of the gases investigated. The following results are fitted using a smooth line function from the C/C_{\max} plots for each of the

five repeat experiments. Figs. 3 and 4 show the noble gases, SF_6 and comparative CO_2 experiments for sandstone flow cell. The five repeated experiments for each pressure are represented as scatter plots. The smooth line functions for each of the pressures are depicted as a solid line.

Table 3 shows the peak breakthrough value of the smooth line functions for each of the tracer pressures. Table 4 shows the mean (including standard deviation) of the five experiments run at each pressure for each tracer mixture. Several consistent trends can be observed when comparing the results of the tracer gas flow through experiments. He is the last of the noble gases to reach C_{\max} for all the pressure ranges and has the narrowest peak shape showing that it is the quickest tracer to cease detection. Ne shows a faster pre-peak concentration arrival but exhibits similar post-peak drop off as He. Ar, Kr and Xe show similar C/C_{\max} timings at lower pressure gradients. As sampling pressures decreases, Kr and Xe continue to have similar pre-peak, C_{\max} and post-peak timings. At all sampling pressures, SF_6 is the fastest to reach C_{\max} and has a broader peak than any of the noble gases, hence taking the longest time to complete flow through the core. CO_2 behaves very differently compared to the noble gases and SF_6 . The CO_2 values never drop close to 0.0 when plotted as C/C_{\max} and take nearly twice as long as the noble gases to reach the C_{\max} . The results show that despite purging the system (all the experiments followed the same procedure), there is a degree of CO_2 retardation. The level of CO_2 does not drop below 'baseline' levels and the retardation processes mask the initial detection breakthrough curves.

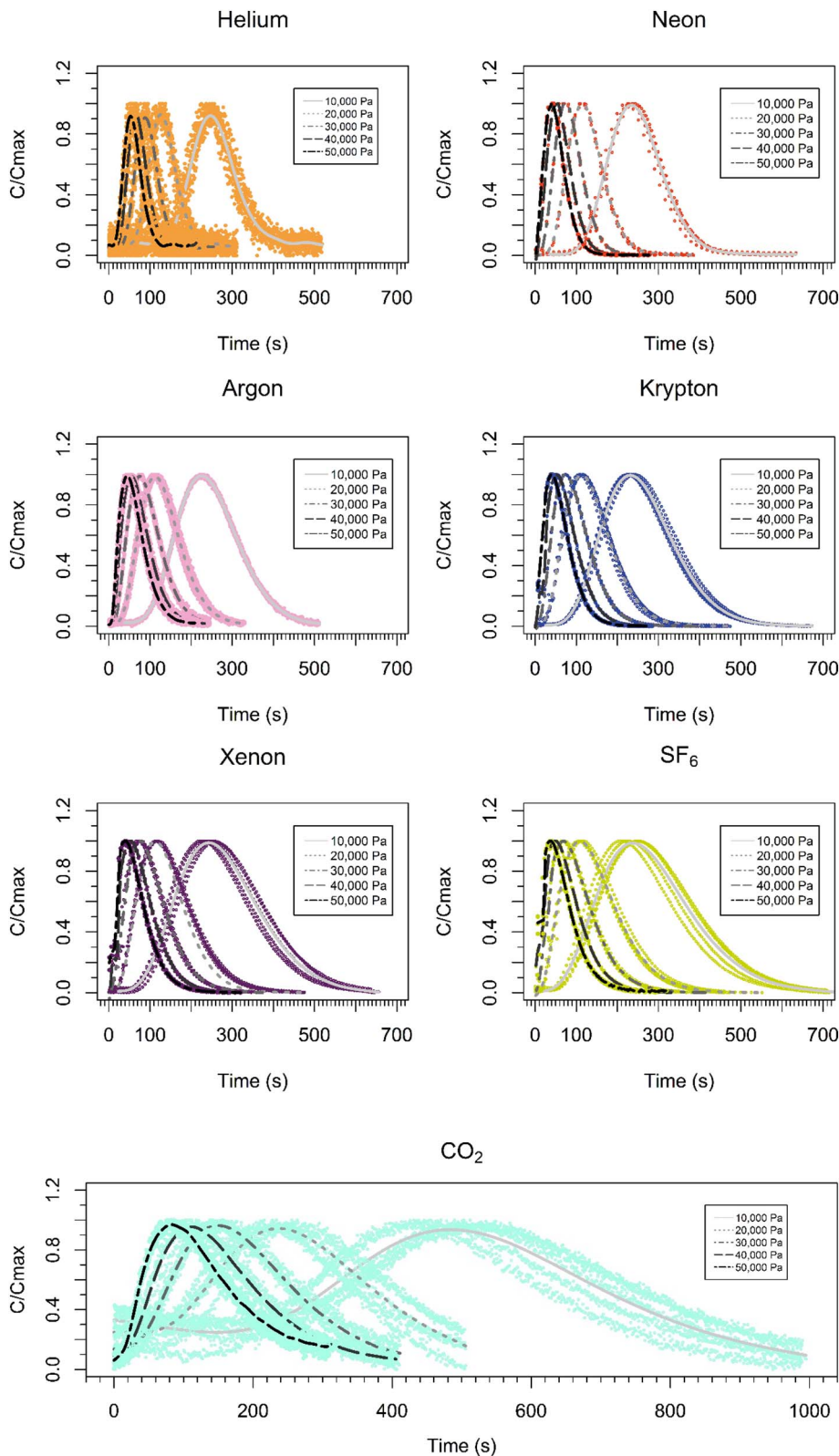


Fig. 3. Scatterplots of flow experiments of He, Ne, Ar, Kr, Xe and SF₆ as discrete gas pulses into CO₂ carrier stream through the flow cell. Smooth lines have been plotted for the gas concentrations (C/C_{\max}) over time (s) as an average of the five experiments.

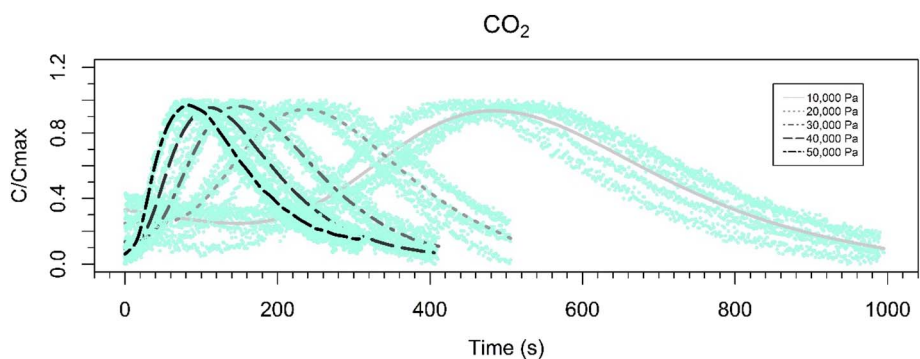


Fig. 4. Results of flow experiments of CO₂ as a discrete gas pulse into N₂ carrier stream through the flow cell. Results are plotted as scatter plots. Smooth lines have been plotted for the gas concentrations (C/C_{\max}) over time (s) as an average of the five experiments.

3.2. Modelling results

Models describing the transport of a tracer in homogeneous porous media can be formulated using a one dimensional advection dispersion transport equation with distance or time dependent transport coefficients. To understand the variables that are involved in the transport of noble gases, SF₆ and CO₂ through the Fell sandstone, a one dimensional

model was applied to the experimental results. The solution of the basic advective dispersion equation used for modelling comparison of the experimental results is:

$$C(x, t) = \frac{M_0}{2\sqrt{\pi D_x t}} \times \exp\left[-\left(\frac{(x - vt)^2}{4D_x t}\right)\right] \quad (2)$$

Table 3

Time (s) of peak breakthrough value using C/C_{\max} for all gases. This value was obtained from the smoothed line fitting to a scatter plot of the five replications of each experiment.

Pressure (kPa)	Peak arrival time (s)						
	He	Ne	Ar	Kr	Xe	SF ₆	CO ₂
50	53	40	45	40	40	38	79
40	65	55	55	51	53	49	112
30	88	70	75	73	75	69	150
20	126	120	113	113	113	108	237
10	247	234	226	230	243	237	483

(e.g. Kinzelbach, 1992).

The modelling of the system was conducted using two complimentary approaches: statistical and analytical using this equation. Table 5 is a summary of the experimental inputs used to construct the modelled breakthrough curves.

3.2.1. Statistically derived transport model

In order to analyse the experimental data and appropriately fit a curve to the results, it is necessary to transform the basic advective dispersion equation into a format that can be easily used to derive values. The advection dispersion equation can be expanded to a linear function with the basic rules of logarithms. The obtained coefficients can be used to determine the advective velocity and dispersion for each example.

The values for permeability were within the expected range for a sample such as sandstone, but the spread of dispersion values is not (Fig. 5, Table 6 and Table 7). Advection is the transport of fluids due to the fluid's bulk motion. In a one dimensional context, it has no effect on the shape of a breakthrough curve. Advection will shift the tracer plume in time by a distance. Dispersion is scale dependent and is the spatial separation of a solute within the matrix (m). Dispersion values are solute and matrix dependent. The cores initial input parameters identified it as a homogenous system with one permeability value associated with it. As such, the dispersivity value (α) should remain the same regardless of the pressure gradient in place as mechanical dispersion is proportional to the magnitude of the advective velocity.

3.2.2. Analytically derived transport model

Based on the output values from the statistical model, an average permeability was identified of $1.01 \times 10^{-12} \text{ m}^2$ ($\pm 2.91 \times 10^{-14} \text{ m}^2$). This value is an average of all the permeability values for each of the gases and pressures (using CO₂ with sorption and excluding Ne due to a poor fit to the modelling results). Porosity was then amended to an average of 17.85%, incorporating both the original experimental derived porosity and the OM images. A singular modelled curve was unable to match the experimental results for all the pressures using a singular dispersivity value. To successfully model the breakthrough curves using the analytical solution, a two-part flow model system was proposed. Although it is possible to propose further complexity, a two-pathway flow model was sufficient for this study.

Table 4

Time (s) of peak breakthrough value using C/C_{\max} for all gases. This value was obtained from the average of the five replications of each experiment.

Pressure (kPa)	Peak arrival time (s)						
	He	Ne	Ar	Kr	Xe	SF ₆	CO ₂
50	54 ± 3	42 ± 2	45 ± 1	40 ± 1	40 ± 2	38 ± 2	82 ± 4
40	63 ± 4	54 ± 5	55 ± 2	52 ± 2	53 ± 1	49 ± 2	110 ± 6
30	87 ± 7	67 ± 6	76 ± 3	73 ± 1	75 ± 3	69 ± 2	150 ± 9
20	129 ± 5	109 ± 1	112 ± 7	113 ± 4	115 ± 2	109 ± 3	239 ± 20
10	242 ± 13	234 ± 8	225 ± 3	233 ± 9	240 ± 15	236 ± 16	485 ± 32

Table 5

Initial modelling inputs for mass transport equation.

Initial modelling inputs	
Average bulk density	2063 kg m ³
Cross sectional area of rock	~0.001 m ²
Dynamic viscosity (CO ₂)	$1.48 \times 10^{-5} \text{ Pa s}^{-1}$
Dynamic viscosity (N ₂)	$1.75 \times 10^{-5} \text{ Pa s}^{-1}$
Flow path length (core)	0.96 m
Temperature (average)	293.15 K
Porosity	17.85%
Pressure	10–50 kPag upstream Ambient pressure downstream

Previous studies of sub-core scale permeability distributions have identified heterogeneity within core samples with similar properties to the Fell sandstone (Krause et al., 2013).

The term 'pathway' was chosen to describe the allocation of the different transport values. However, these two pathways are not independent of one another. Hence, in this context 'pathway' refers to the regions of the pore space matrix that are accessed depending on the pressure gradient applied. Using the statistically derived permeability value of $1.01 \times 10^{-12} \text{ m}^2$ ($\pm 2.91 \times 10^{-14} \text{ m}^2$), the two pathways were designated as 'fast' and 'slow', which are the end members of the permeability range using the deviations values. Based on the relationship between the permeability and the tortuosity of a system, the dispersivity value for pathway one was set to be lower than that of pathway two (Nolen-Hoeksema, 2014). The dispersivity values were identified for each of the gases at 10 kPa and 50 kPa. These values were used as end members to present the generic model for preferential flow channels according to their flow conditions. The simplified relative contribution for each of the pathways as they change flow conditions for all the gases were set the same for each of the pressure gradients (Table 8).

As the advective velocity was determined from the statistical model, this limited the number of variables to the dispersivity values and the relative contribution of the two pathways. To determine the values of the dispersivity, a fixed value was selected that best matched the 50 kPa curve and a different value was selected for the 10 kPa curve as these were the end member gradients (Fig. 6).

The analysis of the breakthrough curves for the tracers implies that all of the tracers have the same advective velocity values over each of the sampling pressures. Therefore, the difference in the width of the breakthrough curves is due to hydrodynamic dispersion, which must differ for each tracer. With the noble gases, He exhibits the least amount of spreading over time and as the atomic radius gets larger towards Xe the width of the flow curve profile increases. Since the calculated values for molecular diffusion are small, mechanical dispersion must be the dominant factor in curve shape. This suggests that there is a higher degree of dispersion with an increase in atomic size, which is confirmed by the modelling results in this study and previous work (Warr et al., 2015).

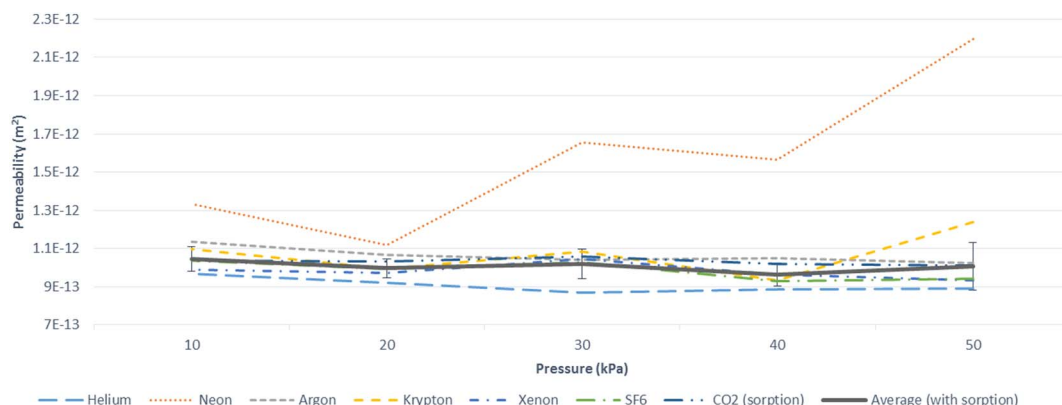


Fig. 5. Combined results for the calculated permeability of the flow cell. Due to its poorly related raw outputs, the values for Ne were not included when calculating the average permeability value.

Table 6

Dispersivity values (m) for all the noble gases and SF₆ at each of the sampling pressures. Dispersivity is calculated where $D_x = n_e D + \alpha |v|$ using the FSG method to determine molecular diffusion (Lyman, 1982).

Pressure (kPa)	Dispersivity (m)					
	He	Ne	Ar	Kr	Xe	SF ₆
50	0.06	0.48	0.17	0.22	0.18	0.17
40	0.05	0.24	0.15	0.12	0.15	0.13
30	0.04	0.19	0.11	0.14	0.14	0.16
20	0.03	0.08	0.08	0.06	0.10	0.11
10	0.03	0.10	0.05	0.06	0.06	0.10

Table 7

Dispersivity values (m) for each of the repeated CO₂ experiments at the different sampling pressures. Each experiment has been modelled individually due to variance in output profiles. Dispersivity is calculated where $D_x = n_e D + \alpha |v|$ using the FSG method to determine molecular diffusion (Lyman, 1982).

Pressure (kPa)	Dispersivity (m)				
	(1)	(2)	(3)	(4)	(5)
50	0.21	0.22	0.19	0.22	0.21
40	0.17	0.18	0.14	0.21	0.18
30	0.13	0.09	0.16	0.14	0.14
20	0.06	0.11	0.11	0.09	0.10
10	0.06	0.07	0.08	0.07	0.06

Table 8

Summary of relative contribution of the two pathways depending on the experimental pressure gradient.

Weighting	Pressure (kPa)
≤ 1:99 ±	50
10:90	40
30:70	30
50:50	20
90:10	10

4. Discussion

4.1. A proposed transport model for the experimental system

SEM images were used in a digital rock reconstruction methodology to generate a 3D model of the rock and infer the pore space using the pore architecture modelling (PAM) as developed by Wu et al. (2006). 3D models generated by this technique can be used in a multiphase flow simulator to determine the multiphase flow dynamics as well as

understand the geometry and topological properties of the pore system. For this research, a PAM can be used to further understand the variations in fluid pathways occurring with a change in image/model scale.

The sample was considered as internally uniform, so a single image was used to generate a PAM. Two BS images at different magnifications of 200 μm and 500 μm (with resolutions of 1.005 μm/pixel and 2.05 μm/pixel) were selected and used to generate two individual 3D PAMs (Fig. 7). A digital pore network was extracted from each model before flow simulation was performed (Wu et al., 2006). Primary drainage was assessed through the injection of oil into an initially water-saturated medium and Fig. 7 shows the extracted pore network from each model after undergoing primary drainage. Here, the blue nodes and bonds are water saturated and the red nodes and bonds are oil saturated. From the visualisation of these flow simulations, differences in the pore network and fluid flow properties can be observed. In the lower resolution model (2.05 μm/pixel), it is apparent that the injected oil does not equally invade all the pore spaces, suggesting that there may be preferential pathways. These preferential pathways appear to have some tortuous behaviour associated with them. With an increase in resolution (1.005 μm/pixel), it is apparent that the oil injection can become impeded and trapped between grains. A potential reason for this is the oil is unable to overcome the capillary threshold pressure. In order to access additional pore spaces during fluid transport, an increase in pressure to overcome the increased capillary threshold is required to enter these pathways.

Using the observed breakthrough curves for the sampling system along with the modelled transport values, it is clear that a simple single pathway model is not sufficient to describe the flow behaviour of the tracers. Based on the two-end member pathway concept that allows resolution of an analytical output to match the data, we now present a discussion of what these findings implicate for a supposed simple homogenous system.

The pathways may be summarised as:

Pathway one, the ‘fast pathway’. It has a higher permeability value of $1.04 \times 10^{-12} \text{ m}^2$ with a porosity of 17.85%. However, the dispersivity value for the pathway is always lower than that of the second proposed pathway. Pathway one is the dominant pathway when the pressure gradient is low.

Pathway two, the ‘slow pathway’. It has a lower permeability value of $9.77 \times 10^{-13} \text{ m}^2$ with a porosity of 17.85%. The dispersivity value of this pathway is higher and is the dominant pathway for the higher pressure gradient.

Darcy’s law describes the flow of fluid through a porous medium. It is the proportional relationship between flow rate, viscosity and changes in pressure over a given distance. Linear flow paths are assumed in Darcy’s Law – a flow regime characterised by parallel flow lines within a system. Linear flow is plotted as a positive $\frac{1}{2}$ slope when time is calculated against pressure (log-log). With Darcy’s flow it is

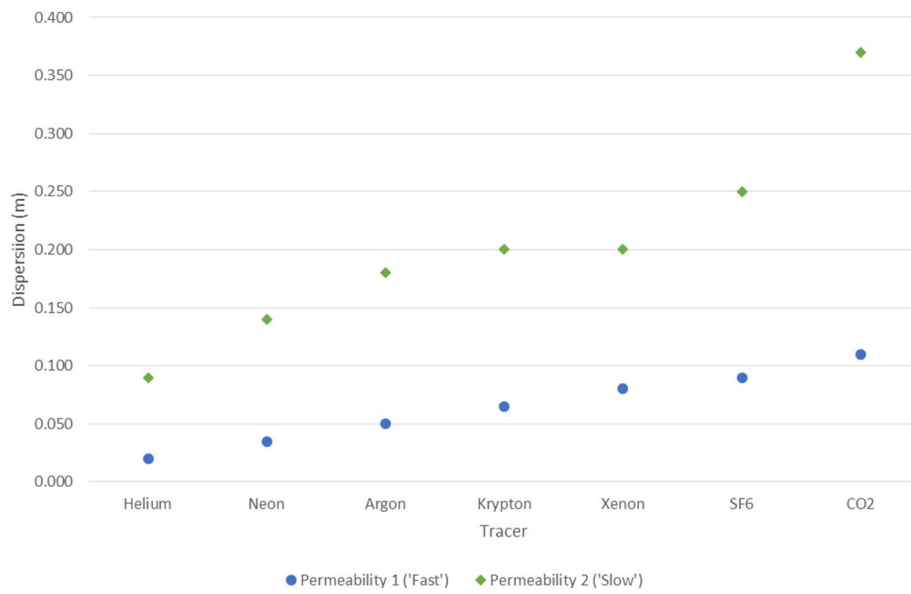


Fig. 6. Using the statistically derived permeability value of $1.01 \times 10^{-12} \text{ m}^2$ ($\pm 2.91 \times 10^{-14} \text{ m}^2$), the two pathways were designated as 'fast' and 'slow' so that they are the end members of the permeability range using the deviations values. The dispersion values estimated for pathways with permeability 1 ($1.04 \times 10^{-12} \text{ m}^2$) and permeability 2 ($9.77 \times 10^{-13} \text{ m}^2$) for each of the tracers are shown here.

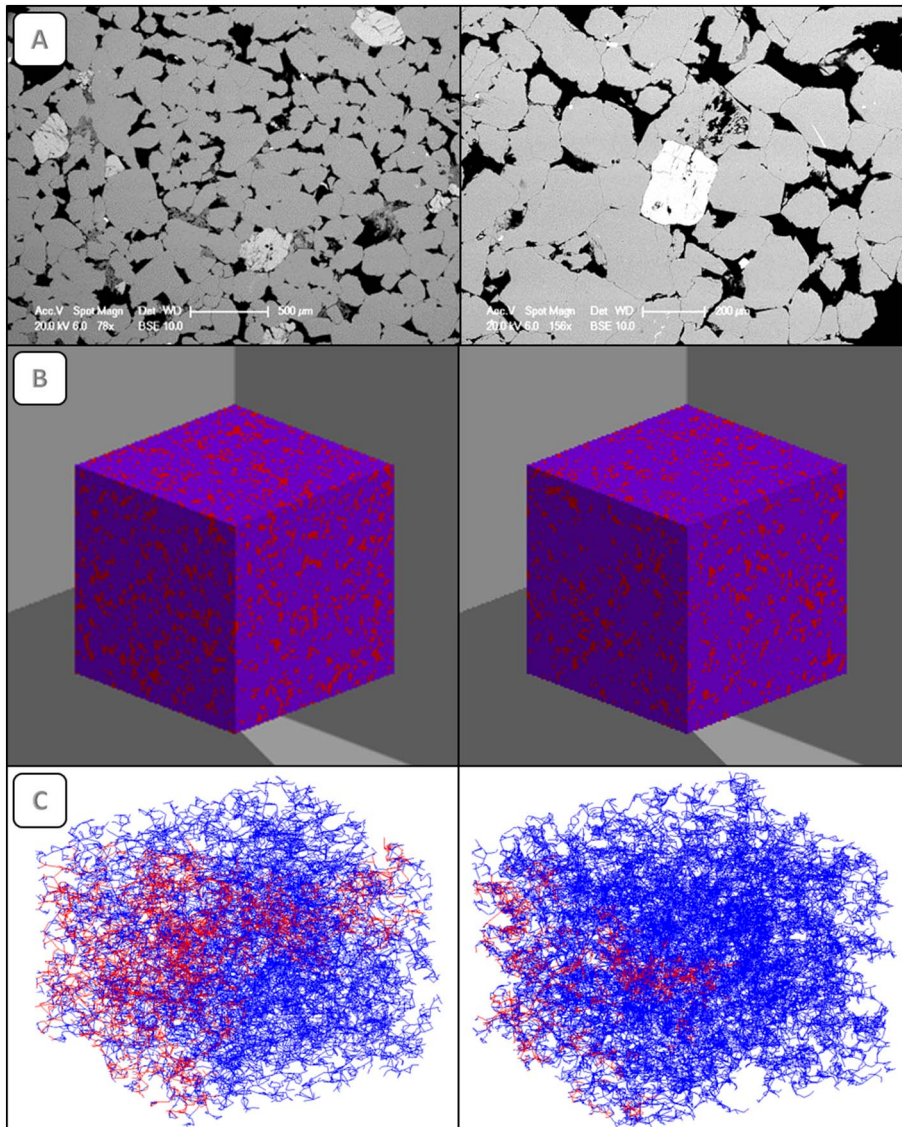


Fig. 7. Results from pore architecture modelling using two BS images to generate digital reconstructions. Each column represents a separate original image and final model. (A) Original BS images used to generate the PAMs. (B) 3D model generated using the BS images. (C) Drainage simulation within the pore network extracted from each PAM.

assumed that the flow is inertialess. Thus, Darcy flow is described as linear, where it accounts for creeping flow and viscous forces prevail over inertial forces.

The Reynolds number (Re) can be used to predict similar flow patterns in different flow scenarios. The dimensionless number can be described as the ratio of inertial forces to viscous forces and be presented as:

$$Re = \frac{g_f v_f L}{\mu} \quad (3)$$

A departure from Darcy regime occurs at order unity ($Re \gg 1$) (Dukhan et al., 2014; Kolditz, 2001). The order of critical Reynolds numbers, when non-linear effects become evident is 1–10 based on previously conducted experiments (Barenblatt et al., 1990). According to Scheidegger (1963), there appear to be two critical Reynolds numbers at which the flow regime changes. The first indicates when the flow conditions are affected by inertia effects and the second when true turbulence flow sets in (Dullien, 2012).

Before a flow becomes turbulent, non-linear laminar effects occur and flow deviates from a Darcy regime (Kolditz, 2001) (Fig. 8). Non-linear laminar flow becomes the dominant method of flow as inertial effects become important. Causes of non-linear effects can be high advective velocity, molecular/ionic effects, non-Newtonian behaviour of the fluid itself as well as pore geometry (Kolditz, 2001; Dullien, 2012; Scheidegger, 1963). Forchheimer's Law includes the inertial effect as a function of the kinetic energy in the relationship between the pressure gradient and the flow velocity such that:

$$-\frac{dP}{dx} = \frac{\mu}{k} v + \beta \rho v^2 \quad (4)$$

As flow velocity increases, the kinetic energy term becomes more important and the linear relationship breaks down. The determination of the Forchheimer coefficient tends to be calculated using the best-fit information from experimental data. The Forchheimer coefficient is strongly dependent on the internal structure of the porous medium (Dukhan et al., 2014). Previous work has shown that for the same porous medium, different values of permeability exist in different flow regimes (Dukhan et al., 2014).

Using the Forchheimer equation, Kolditz (1997, 2001) represents this breakdown of linear behaviour as:

$$q = K |\Delta i|^{(\alpha^*-1)} = K_0 K_{rel} \quad (5)$$

To fully understand the implications of our results we now focus on the pathway functions and contributions at each pressure gradient. Table 9 shows the estimated Re values for the Fell sandstone system. Values were calculated using the average advective velocity for the system over the sampling pressure gradients. The characteristic length scale for porous media is based on grain boundary diameters. Re numbers were calculated for two pore space diameters (450 and 150 μm derived from ImageJ analysis). Pathway one was allocated the maximum detected pore diameter range of 450 μm due to the higher permeability value and lower dispersivity trend – permeability is directly related to pore space/grain size. Similarly, pathway two was allocated diameter value of 150 μm as this was calculated as the most dominant size for diameter. For comparative purposes, the relative contribution allocated to both pathways during modelling are included.

Any flow with a Re approaching 1 suggests a transition into non-linear laminar flow. Reynolds numbers for turbulent flow are much higher than anything that are produced during the experimental conditions.

a) Low pressure (10 kPa)

At low sampling pressure gradients, the flow contribution is primarily via pathway one. The flow passes through the higher permeability portions of the system with greater ease and these are the areas

of higher pore diameter. At the low sampling pressure gradient, the Re values suggest that the flow is following the Darcy regime and as such is pure linear laminar flow. At this pressure gradient level, there appears to be little or no contribution flow through the higher dispersivity routes (pathway two).

b) Medium pressure (20–30 kPa)

With an increase in pressure gradient, there is a distinct increase in Re numbers for pathway one and approaches the value of unity. The contribution from both pathways has become 50:50 at 20 kPa. Within the 30 kPa pressure gradient, pathway one approaches non-linear laminar flow. Pathway two remains within the region of linear laminar flow. As such, the medium pressure gradient range is a transition of areas with linear and non-linear laminar flow.

c) High pressure (40 kPa to 50 kPa)

When the pressure gradient reaches 40 kPa, the contribution of flow is predominately through pathway two. The lower permeability pathway two is providing 90% of the tracer route contribution through a more dispersive manner, reducing the contribution from the higher permeability regions. By 50 kPa, the contribution of the pathway one has drastically reduced and according to the Re is well into the non-linear laminar flow region. At this pressure, the linear flow is approaching unity but accounts for 90% of the flow.

As suggested in Dukhan et al. (2014) permeability within a Darcy regime is considered constant, while in the Forchheimer regime, it decreases with increasing velocity. This observation agrees with the modelling output descriptions when compared to the Re numbers of those areas. Thus, it appears that within this Fell sandstone core, the transition from linear to non-linear flow on the micro-scale (no turbulent regions), is the reason for identifying multiple pathways or routes that are taken by the tracer as the velocity increases. Fig. 9 summarises the different areas of the flow cell, which are accessed depending on the advective velocity. These areas have been classified as pathway one and two but these regions are not isolated as depicted in Fig. 9.

4.2. Implications for using tracers to track CO_2 migration

The main advantages of chemical tracers are that they can be used to make measurements in natural field settings that are impossible to access physically and can cover large scales. Monitoring injected CO_2 can be challenging, as it is a reactive compound, highly soluble and subject to multiple phases depending on pressure and temperature changes. Thus, the use of chemical tracers that have limited interactions with the injection fluids and surrounding reservoir are the dominant choice; they track fluid pathways of migration but should do so

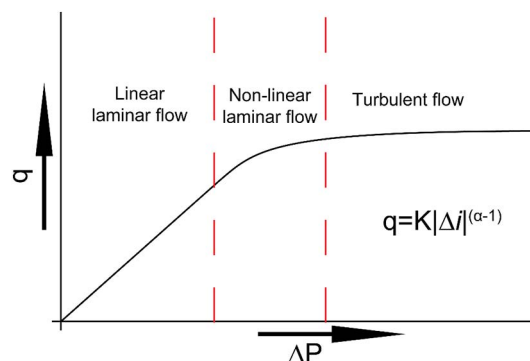


Fig. 8. Not-to-scale illustration representing the different flow regimes found as a relationship between pressure (ΔP) and flow rate (q), using the non-linear flow parameter (α^*).

Table 9

Reynolds number for CO₂ transport through the Fell sandstone under experimental conditions. For comparative purposes, the relative contribution allocated to both pathways during modelling are included.

Pressure gradient (kPa)	Pathway one (%)	Pathway one (<i>Re</i>)	Pathway two (%)	Pathway two (<i>Re</i>)
High Pressure	50 ≤ 1	1.92	99 ±	0.64
	40 10	1.27	90	0.42
Medium Pressure	30 30	0.94	70	0.31
	20 50	0.52	50	0.17
Low Pressure	10 90	0.26	10	0.09

conservatively. The timing of the tracers should be predictable to the point that a clear pattern emerges in relation to the migration of CO₂. This research investigated the possibility of fractionation of tracers through natural processes, leading to some tracers being detectable very early in the release of CO₂, and others being delayed.

4.2.1. Noble gases as early warning tracers for CO₂ migration

As such, there are two approaches to deciding how these tracers could be used as an early warning tracer for CO₂ migration. Firstly, using these timings, it is evident that all the noble gases and SF₆ reach C_{max} before CO₂ does. This suggests that all the noble gases and SF₆ can be successful tracers for identifying the early migration of CO₂ under the experimental conditions.

Alternatively, when a baseline has been identified prior to injection, the initial arrival of certain tracers could be used as early warning indicators for possible CO₂ migration. From this approach, it is apparent that He, Ne and Ar may not be suitable as early warning tracers for CO₂ migration. Kr and Xe arrival times are significantly ahead of CO₂ and hence could be used as an early warning means of detecting CO₂ migration. The results suggest that SF₆ is the fastest travelling tracer for pre-peak concentration values.

4.2.2. Noble gases as a method of fingerprinting CO₂ storage sites

While He, Ne and Ar appear to be unsuitable as early warning tracers for initial detection of CO₂, our findings suggest that they can be

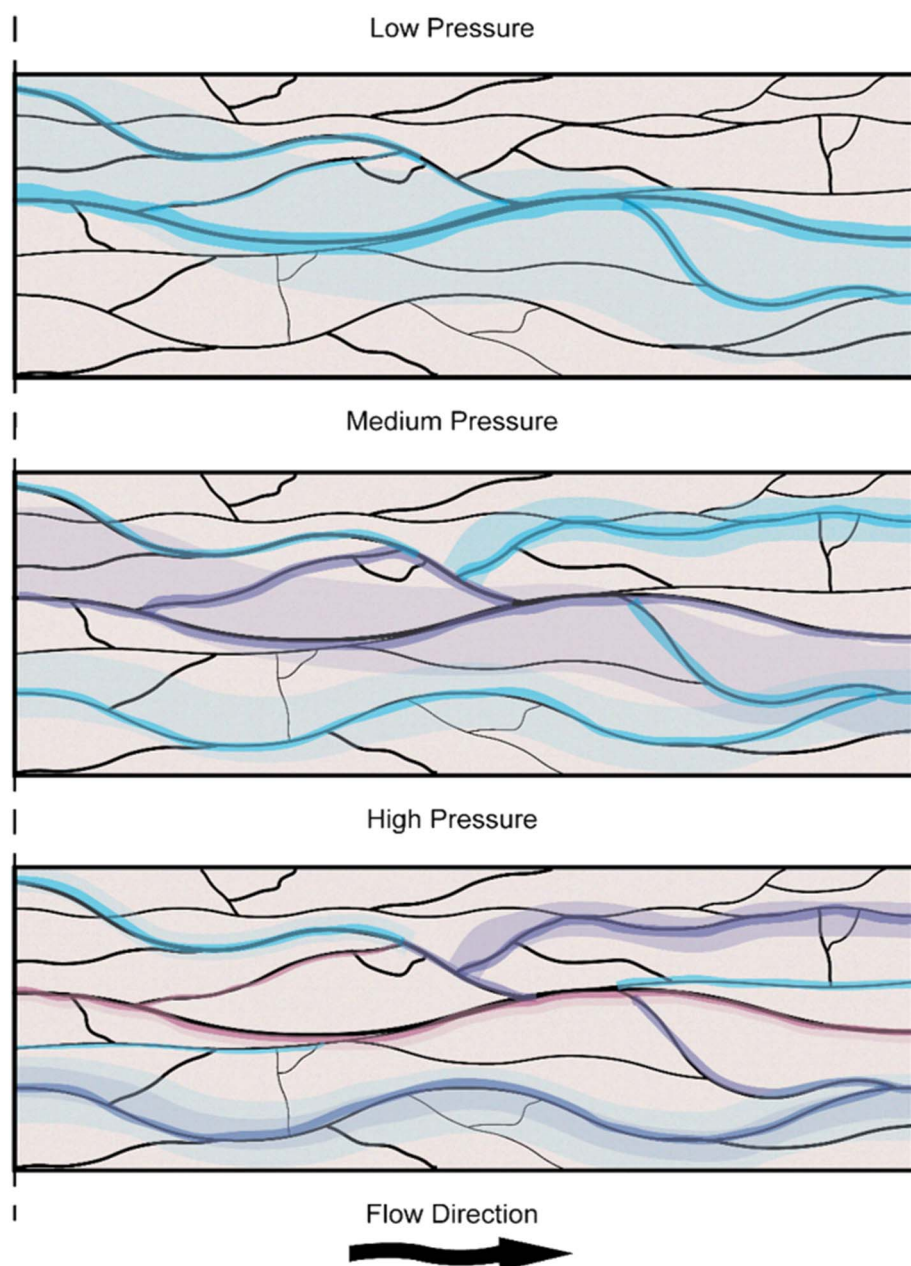


Fig. 9. Schematic diagram illustrating the different contributing areas of the flow cell, as there is an increase in flow velocity. The blue areas represent linear laminar flow, the purple areas represent a transition to non-linear laminar flow and the red areas are non-linear laminar flow. (For interpretation of the references to colour in this figure legend, the reader is referred to the web version of this article.)

used as part of mixture to fingerprint individual CO₂ storage sites that may be in close proximity to one another. Noble gases and their isotopes are able to provide unique constraints on certain geological processes (Gilfillan et al., 2014; Burnard et al., 2013; Holland and Gilfillan, 2012; Wilkinson et al., 2010; Gilfillan et al., 2008; Gilfillan et al., 2017). Understanding their predicted arrival times in relation to each other can help determine ownership of CO₂ storage sites and thus the party responsible to rectify any unplanned effects.

4.2.3. How do these results compare to reservoir scale test sites?

The fundamental aim of the project was to understand the mechanisms involved for the transport of tracers in porous media. We have uncovered that there are considerable differences in the behaviour of ‘conservative’ noble gases as tracers and contributed to the understanding of transport at the micro-pore scale. The experiments for this research were carried out under a low range of pressure gradients, single-phase conditions and through an air-dried sample. Upscaling these conditions directly to real world environments where CO₂ storage is carried out in underground environments with multiphase flow and high-pressure conditions needs further investigation. However, by identifying any similarities in the results from this research to real world environments, it can help answer some of the uncertainties raised in the larger scale experiments.

The research of Carrigan et al. (1996) presented the transport of ³He and SF₆ tracer gas flow along faults and fractures, following their release underground at a depth of 400 m, resulting from barometric pressure variations. These fractures may be considered as preferential pathways during transport. From these results, SF₆ arrived at the monitoring stations at the surface after 50 days, with ³He taking 375 days, though the initial detection location was the same for both tracers. In a diffusively dominated transport environment, the ³He should have arrived before the SF₆ based on atomic size. Carrigan et al. (1996) suggests that the speed of transport along the fractures is much greater than the diffusion rate driven by deeper ‘low’ barometric pressure variations. They also suggest that the high diffusion coefficient of He compared to SF₆ actually impedes its transport along a fracture by allowing it to diffuse out of the main flow path more effectively than SF₆. This observation is analogous to our findings and potentially helps to explain why He is the slowest tracers to arrive during all pressure gradients and also how it is the quickest to drop below detection levels following post-peak concentration, with matrix diffusion acting in the same way as grain sorption would.

The choice of using Kr with SF₆ has proven to be popular for monitoring CO₂ pathways. The Cranfield Enhanced Oil Recovery field in Mississippi is home to a large-scale CO₂ injection and observation survey from a natural source (Jackson Dome), which has been used for data collection and monitoring (Hovorka et al., 2013). Lu et al. (2012) carried out CO₂ and tracer fluid sampling in two observation wells, located 100 and 200 ft. horizontally from the CO₂ injection well in the same reservoir formation. This was undertaken in the water leg of an isolated down-dip portion of the reservoir during CO₂ injection in 2009 and 2010. SF₆ and Kr were added to the injected CO₂ and the breakthrough of the CO₂, SF₆ and Kr was recorded via intensive sampling of the reservoir fluids through a down-hole U-tube sampling system in December 2009 and in April 2010. In the first tracer injection, SF₆ arrived before Kr at both observation wells. In the December 2009 test, the tracers arrived at the well nearest to the CO₂ injection well first. An increase in injection rate led to a second pulse of Kr arriving but not SF₆ – perhaps the result of their physical or chemical properties. During the second injection of tracer following an increase in both injection rate and fluid flow velocity, the SF₆ arrived at the more-distant observation well earlier than the closer one. These results highlight the possibility of separate flow pathways existing between wells and that travel time is not proportional to the distance between the wells, with fluid velocities being variable along different flow pathways.

There are a number of similarities between the result from these full scale experiments in Cranfield and our laboratory scale results. In terms of peak concentration, Kr arrives later than the SF₆ at the sampling pressure gradients and also ceases detection before SF₆, which is similar to the observations at Cranfield during the December 2009 tracer experiments. In both experiments it is clear that the flow velocities of each tracer depends non-linearly on the density/viscosity and hence imply that preferential flow paths can exist. Although in the case of Cranfield, they consider these paths as separate and distinct, most likely due to the larger scale of the system.

5. Conclusions

Tracers mixed with injected CO₂ could act as fingerprints for ownership resolution, and as early warnings of migration into receptor wells, ahead of CO₂. This study involved experiments that injected individual noble gases, and the benchmark tracer SF₆, through a core of sandstone saturated with gaseous CO₂. Concentrations of the tracers were measured through time at the downstream end of the core. Imposed pressure gradients were 10–50 kPa m⁻¹. Although noble gases are described as conservative tracers, comparing the breakthrough curves over a range of pressure gradients show that they do not behave as simply as previously assumed. The arrival times of Kr and Xe were similar to SF₆ indicating that it could be substituted for future tracer applications. Smaller molecules of He are diverted into disconnected and dead-end pores, which are avoided by larger molecules. Importantly, we have successfully modelled the experimental results using a one dimensional advection dispersion model. With these results, a conceptual model has been constrained for the experimental system whereby preferential paths exist depending on the flow velocity. At the low pressure gradient, the system follows a Darcy flow regime and tracers travel preferentially along a higher permeability route. With an increase in pressure, *Re* values suggest a partial migration from a linear to a non-linear regime at the pore diameter scale. By 50 kPa gradient, higher permeability pathways are experiencing non-linear laminar flow but contribute significantly less to the overall route. The low permeability regimes with a higher dispersivity are the dominant pathway. This suggests that an increase in *Re* number leads to a non-linear laminar flow, which is ‘slower’ to contribute than a true linear laminar flow to the Fell sandstone system. These results can be used to explain patterns observed with tracers in large-scale reservoirs.

Acknowledgements

Rachel Kilgallon was funded by the Scottish Power Academic Alliance and the Scottish Energy Technology Partnership for this project. Stuart Gilfillan was supported by a Natural Environmental Research Council (NERC) Postdoctoral Fellowship, grant NE/G015163/1 for part of this work, and is currently funded by EPSRC, NERC and the EU. Katriona Edlmann is funded by the EU and ICCR. Christopher McDermott is funded by the EU and SCCS. Stuart Haszeldine is funded by SCCS, EPSRC, NERC, Scottish Power, Scottish Funding Council, and a consortium of power and CO₂ storage companies. The research leading to these results has received funding from the European Community's Seventh Framework Programme FP7/2007-2013 under the grant agreement No. 282900 as part of the PANACEA project. The authors have no shareholdings or other competing interests. Particular acknowledgements to Dr. Zeyun Jiang, at the Institute of Petroleum Engineering, Heriot-Watt University for generation of the PAM. Additional acknowledgements to Core Laboratories for contributing to the flow cell construction. We acknowledge the constructive comments from Magali Pujol and an anonymous reviewer, along with editorial handling by Pierre-Henri Blard, which greatly improved the manuscript.

Appendix A. Supplementary data

Supplementary data to this article can be found online at <http://dx.doi.org/10.1016/j.chemgeo.2017.09.022>.

References

- Anselmetti, F.S., Luthi, S., Eberli, G.P., 1998. Quantitative characterization of carbonate pore systems by digital image analysis. *AAPG Bull.* 82, 1815–1836.
- Azar, C., Lindgren, K., Obersteiner, M., Riahi, K., van Vuuren, D.P., Den Elzen, K.M.G.J., Möllersten, K., Larson, E.D., 2010. The feasibility of low CO₂ concentration targets and the role of bio-energy with carbon capture and storage (BECCS). *Climate Change* 195–202.
- Barenblatt, G., Entov, V., Ryzhik, V., 1990. *Theory of Fluid Flows through Natural Rocks*. Kluwer Academic Publishers.
- Bell, F.G., 1978. The physical and mechanical properties of the fell sandstones, Northumberland, England. *Eng. Geol.* 12, 1–29.
- British Geological Survey, 2016. *Fell sandstone formation* [Online]. Available: <http://www.bgs.ac.uk/lexicon/lexicon.cfm?pub=FELL>.
- Burnard, P., Zimmermann, L., Sano, Y., 2013. The noble gases as geochemical tracers: history and background. In: *The Noble Gases as Geochemical Tracers*. Springer.
- Carman, P.C., 1956. *Flow of Gases Through Porous Media*. Butterworths Scientific Publications, London.
- Carrigan, C.R., Heinle, R.A., Hudson, G.B., Nitao, J.J., Zucca, J.J., 1996. Trace gas emissions on geological faults as indicators of underground nuclear testing. *Nature* 383, 528–531.
- van Der Land, C., Wood, R., Wu, K., van Dijke, M.I.J., Jiang, Z., Corbett, P.W.M., Couples, G., 2013. Modelling the permeability evolution of carbonate rocks. *Mar. Pet. Geol.* 48, 1–7.
- Dukhan, N., Bağcı, Ö., Özdemir, M., 2014. Experimental flow in various porous media and reconciliation of Forchheimer and Ergun relations. *Exp. Thermal Fluid Sci.* 57, 425–433.
- Dullien, F.A., 2012. *Porous Media: Fluid Transport and Pore Structure*. Academic press.
- Edlmann, K., Haszeldine, S., Mcdermott, C., 2013. Experimental investigation into the sealing capability of naturally fractured shale caprocks to supercritical carbon dioxide flow. *Environ. Earth Sci.* 70, 3393–3409.
- Flude, S., Johnson, G., Gilfillan, S.M.V., Haszeldine, R.S., 2016. Inherent tracers for carbon capture and storage in sedimentary formations: composition and applications. *Environ. Sci. Technol.* 50 (15), 7939–7955. <http://pubs.acs.org/doi/abs/10.1021/acs.est.6b01548>.
- Flude, S., Györe, D., Stuart, F.M., Zurakowska, M., Boyce, A.J., Haszeldine, R.S., Chalaturnyk, R., Gilfillan, S.M.V., 2017. The inherent tracer fingerprint of captured CO₂. *Int. J. Greenhouse Gas Control* 65, 40–54.
- Gilfillan, S.M.V., Ballentine, C.J., Holland, G., Blagburn, D., Lollar, B.S., Stevens, S., Schoell, M., Cassidy, M., 2008. The noble gas geochemistry of natural CO₂ gas reservoirs from the Colorado Plateau and Rocky Mountain provinces, USA. *Geochim. Cosmochim. Acta* 72, 1174–1198.
- Gilfillan, S.M., Lollar, B.S., Holland, G., Blagburn, D., Stevens, S., Schoell, M., Cassidy, M., Ding, Z., Zhou, Z., Lacrampe-Couloume, G., Ballentine, C.J., 2009. Solubility trapping in formation water as dominant CO₂ sink in natural gas fields. *Nature* 458, 614–618.
- Gilfillan, S.M.V., Haszeldine, R.S., Stuart, F.M., Györe, D., Kilgallon, R., Mark Wilkinson, M., 2014. The application of noble gases and carbon stable isotopes in tracing the fate, migration and storage of CO₂. *Energy Procedia* 63, 4123–4133.
- Gilfillan, S.M.V., Sherk, G.W., Poreda, R., Haszeldine, R.S., 2017. Using noble gas fingerprints at the Kerr Farm to assess CO₂ leakage allegations linked to the Weyburn-Midale CO₂ monitoring and storage project. *Int. J. Greenhouse Gas Control* 63, 215–255.
- Györe, D., Stuart, F.M., Gilfillan, S.M.V., Waldron, S., 2015. Tracing injected CO₂ in the Cranfield enhanced oil recovery field (MS, USA) using He, Ne and Ar isotopes. *Int. J. Greenhouse Gas Control* 42, 554–561.
- Györe, D., Gilfillan, S.M., Stuart, F.M., 2017. Tracking the interaction between injected CO₂ and reservoir fluids using noble gas isotopes in an analogue of large-scale carbon capture and storage. *Appl. Geochem.* 78, 116–128.
- Haszeldine, R.S., 2009. Carbon capture and storage: how green can black be? *Science* 325, 1647–1652.
- Holland, G., Gilfillan, S.M.V., 2012. Application of noble gases to the viability of CO₂ storage. In: *The Noble Gases as Geochemical Tracers*, pp. 177–223.
- Hovorka, S.D., Meckel, T.A., Trevino, R.H., 2013. Monitoring a large-volume injection at Cranfield, Mississippi—project design and recommendations. *Int. J. Greenhouse Gas Control* 18, 345–360.
- Hutton Stone Co. Ltd., 2013. *Hazeldean. technical information* [Online]. Available from: <http://www.huttonstone.co.uk/guides/hazeldean.pdf>.
- IPCC, 2015. *Climate Change 2014: Mitigation of Climate Change. Vol. 3 Cambridge University Press*.
- Jenkins, C.R., Cook, P.J., Ennis-King, J., Underschlutz, J., Boreham, C., Dance, T., de Caritat, P., Etheridge, D.M., Freifeld, B.M., Hortle, A., Kirste, D., 2012. Safe storage and effective monitoring of CO₂ in depleted gas fields. *Proc. Natl. Acad. Sci.* 109 (2), E35–E41.
- Kinzelbach, W., 1992. *Numerische Methoden zur Modellierung des Transports von Schadstoffen im Grundwasser*. München, Oldenbourg Verlag.
- Kolditz, O., 1997. *Strömung, Stoff- und Wärmetransport im Kluffgestein*, Borntraeger Berlin, Stuttgart.
- Kolditz, O., 2001. Non-linear flow in fractured rock. *Int. J. Numer. Methods Heat Fluid Flow* 11, 547–575.
- Krause, M., Krevor, S., Benson, S.M., 2013. A procedure for the accurate determination of sub-core scale permeability distributions with error quantification. *Transp. Porous Media* 98, 565–588.
- Mioic, et al., 2016. Controls on CO₂ storage security in natural reservoirs and implications for CO₂ storage site selection. *Int. J. Greenhouse Gas Control* 51, 118–125 August.
- Liu, Y., Larson, T.E., Nicot, J.-P., 2014. Theoretical and experimental study of controls on CO₂ dissolution and CH₄ outgassing rates. *Energy Procedia* 63, 4773–4781.
- Lu, J., Cook, P.J., Hosseini, S.A., Yang, C., Romanak, K.D., Zhang, T., Freifeld, B.M., Smyth, R.C., Zeng, H., Hovorka, S.D., 2012. Complex fluid flow revealed by monitoring CO₂ injection in a fluvial formation. *J. Geophys. Res. Solid Earth* 117, 117.
- Lyman, W.J., 1982. *Handbook of Chemical Property Estimation Methods*. American Chemical Society.
- Mccallum, S.D., Riestenberg, D.E., Cole, D.R., Freifeld, B.M., Trautz, R.C., Hovorka, S.D., Phelps, T.J., 2005. Monitoring geologically sequestered CO₂ during the Frio Brine pilot test using perfluorocarbon tracers. In: *Proceedings, Fourth Annual Conference on Carbon Capture and Sequestration DOE/NETL*.
- Myers, M., White, C., Stalker, L., Ross, A., 2012. *Literature Review of Tracer Partition Coefficients*.
- Myers, M., Stalker, L., Pejčić, B., Ross, A., 2013. Tracers—past, present and future applications in CO₂ geosequestration. *Appl. Geochem.* 30, 125–135.
- Nimz, G.J., Hudson, G.B., 2005. The use of noble gas isotopes for monitoring leakage of geologically stored CO₂. In: *Carbon Dioxide Capture for Storage in Deep Geologic Formations. vol. 2. pp. 1113–1128*.
- Nolen-Hoeksema, R., 2014. Flow through pores. *Oilfield Rev. Autumn* 26.
- Reynolds, C.A., Menke, H., Andrew, M., Blunt, M.J., Krevor, S., 2017. Dynamic fluid connectivity during steady-state multiphase flow in a sandstone. *Proc. Natl. Acad. Sci.* 201702834.
- Sathaye, K.J., Hesse, M.A., Cassidy, M., Stockli, D.F., 2014. Constraints on the magnitude and rate of CO₂ dissolution at bravo dome natural gas field. *Proc. Natl. Acad. Sci. U. S. A.* 111, 15332–15337.
- Scheidegger, A.E., 1963. *Physics of flow through porous media*. In: *Physics of Flow through Porous Media*. University of Toronto.
- Scott, V., Gilfillan, S., Markusson, N., Chalmers, H., Haszeldine, R.S., 2013. Last chance for carbon capture and storage. *Nat. Clim. Chang.* 3, 105–111.
- UNFCCC, 2015. *Adoption of the Paris Agreement. Report No. FCCC/CP/2015/L.9/Rev.1*. <http://unfccc.int/resource/docs/2015/cop21/eng/109r01.pdf>.
- Warr, O., Rochelle, C.A., Masters, A., Ballentine, C.J., 2015. Determining noble gas partitioning within a CO₂–H₂O system at elevated temperatures and pressures. *Geochim. Cosmochim. Acta* 159, 112–125.
- Wilkinson, M., Gilfillan, S.M.V., Haszeldine, R.S., Ballentine, C.J., 2010. *Plumbing the Depths: Testing Natural Tracers of Subsurface CO₂ Origin and Migration, Utah. Carbon Dioxide Sequestration in Geological Media State of the Science (Aapg Studies in Geology)*.
- Wu, K., van Dijke, M.I., Couples, G.D., Jiang, Z., Ma, J., Sorbie, K.S., Crawford, J., Young, I., Zhang, X., 2006. 3D stochastic modelling of heterogeneous porous media—applications to reservoir rocks. *Transp. Porous Media* 65, 443–467.
- Zhou, Z., Ballentine, C.J., Schoell, M., Stevens, S.H., 2012. Identifying and quantifying natural CO₂ sequestration processes over geological timescales: the Jackson dome CO₂ deposit, USA. *Geochim. Cosmochim. Acta* 86, 257–275.